OPEN

Quantum strain sensor with a topological insulator HgTe quantum dot

Marek Korkusinski & Pawel Hawrylak

Quantum Theory Group, Security and Disruptive Technologies Portfolio, Emerging Technologies Division, National Research Council, Ottawa, Canada K1A 0R6.

We present a theory of electronic properties of HgTe quantum dot and propose a strain sensor based on a strain-driven transition from a HgTe quantum dot with inverted bandstructure and robust topologically protected quantum edge states to a normal state without edge states in the energy gap. The presence or absence of edge states leads to large on/off ratio of conductivity across the quantum dot, tunable by adjusting the number of conduction channels in the source-drain voltage window. The electronic properties of a HgTe quantum dot as a function of size and applied strain are described using eight-band $\vec{k}\cdot\vec{p}$ Luttinger and Bir-Pikus Hamiltonians, with surface states identified with chirality of Luttinger spinors and obtained through extensive numerical diagonalization of the Hamiltonian.

There is currently significant interest in using quantum effects to develop capabilities in sensing at the nanoscale, from single-electron charge detection using quantum point contacts[1,2], few nuclear spins using the quantum states of NV center in diamond[3,4] to piezotronic sensors of strain[5,6] and development of smart skin[7]. The piezotronic sensors rely on inducing a charge on the surface of piezoelectric semiconductor nanowire by strain, which in turn continuously changes the conductivity of the nanowire[5]. Here we describe a novel strain sensor based on a strain-driven transition from a HgTe quantum dot with inverted bandstructure and robust topologically protected quantum edge states to a normal state without edge states in the energy gap. The presence/ absence of edge states is expected to lead to large on/off ratio of conductivity across the quantum dot in analogy to recently demonstrated large piezoresistive current on/off ratios driven by a pressure-induced metal/insulator transition in rare earth chalcogenide thin films[8]. The electronic properties of a HgTe quantum dot as a function of applied strain are described using eight-band $\vec{k}\cdot\vec{p}$ theory and surface states are identified with chirality of Luttinger spinors.

The principle of operation of the quantum strain sensor based on a HgTe topological insulator quantum dot is summarized in Fig. 1. Panel (a) shows a thick, finite-size HgTe quantum well in the form of a disk embedded in vacuum or a higher bandgap material such as CdTe. The quantum dot is connected to two metallic electrodes. The quantum well of HgTe is an example of a topological insulator (TI), a material with an energy gap in the bulk, accompanied by helical, topologically protected states at its edge[9–14]. This is in contrast with normal semi-conductor (NS) quantum dot, in which the states from the electron and hole subbands are separated by an empty energy gap[15]. The thickness of the HgTe quantum well, through quantum confinenement, controls the relative position of the s and p bands. As a result, there exists a transition from the inverted to normal bandstructure when the thickness of the quantum well is reduced below the critical thickness H_C. At this special thickness, the quasiparticle in-plane dispersion correponds to a single Dirac cone[13]. The thickness of the disk in Fig. 1 is larger than H_C, which results in the inverted bandstructure and the existence of states, whose energy falls within the gap and probability density peaks at the disk edge[16].

In Fig. 1(a), the red ring represents the computed probability density of one of the edge states. If the Fermi energy of the leads is aligned with the energy of the edge state, electrons are expected to tunnel efficiently from the right to the left lead via the edge state and one detects a high current flow. Assuming ballistic transport, the current I is proportional to the number M of edge states and the applied voltage V_{SD}, $I = G_0 M T V_{SD}$, where G_0 is a quantum of conductance $G_0 = e^2/h$, and T is the transmission coefficient[17–19]. This is schematically visualized as the red line - high current or large number of edge states - in Fig. 1, where we plot the tunneling current as a function of the strain. As we apply strain to our disk, the edges of both s and p bands shift in energy, but with different deformation potentials. If the strain is large enough, the HgTe quantum well bandstructure is no longer inverted and the edge states disappear from the energy gap and are out of the resonance with the Fermi levels of the leads. Since there is no state available for the electrons to tunnel through, the current is expected to vanish, as depicted in Fig. 1 (b). As
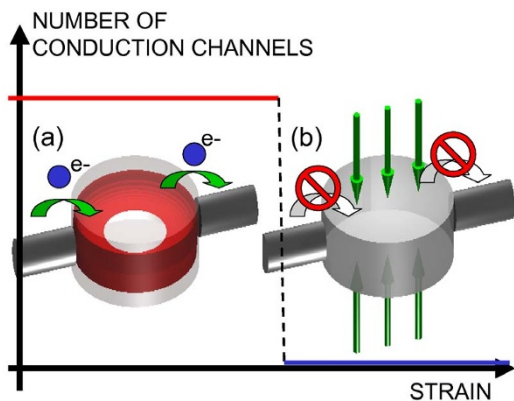
Figure 1 | Schematic explanation of the principle of operation of the strain sensor. (a) The unstrained HgTe disk in the inverted regime is placed between two metallic electrodes. The Fermi energy of the electrodes matches the energy of one of the edge states. The current flows since the electrons tunnel easily into and out of the edge state in the disk. (b) Upon applied vertical stress, the gap opens in the single-particle spectrum of the disk. There are no states matched with the Fermi energy of the leads, the current does not flow.
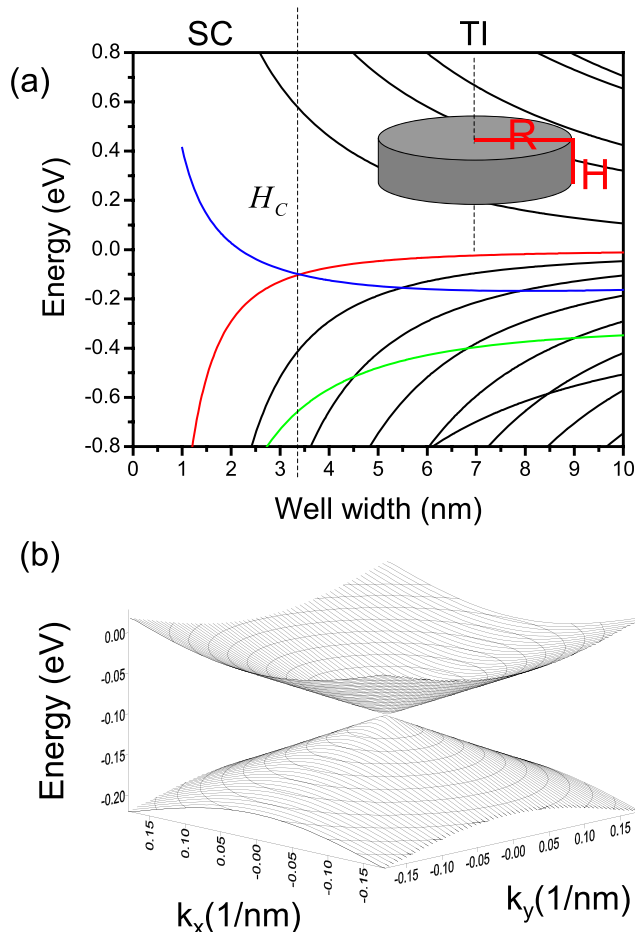

**Figure 2 | (a) Subband edge energies in a HgTe quantum well at $k_x = k_y = 0$ as a function of the well thickness H. H_C denotes the crossing between the lowest conduction (blue) and heavy-hole (red) subband edges, marking the transition between the normal semiconductor and the inverted bandgap material. Inset shows a schematic picture of the system composed of a single, free-standing, disk-shaped HgTe nanocrystal. (b) The in-plane dispersion of the conduction and heavy-hole subbands at the height H_C, showing the characteristic Dirac cone shape.

shown in the main panel, the vanishing of current (blue line) is expected to occur when the strain exceeds the critical value. The robustness and sharpness of edge states is expected to lead to a very high on-off ratio of current as a function of applied strain.

We now turn to a microscopic description of a HgTe quantum dot based on eight-band $\vec{k} \cdot \vec{p}$ theory developed for semiconductor quantum dots[15,20–23], HgTe quantum wells[24] and HgTe colloidal nanocrystals[25–27]. We note that a simplified model of a strictly two-dimensional quantum disk embedded in vacuum and described by a heavy hole and conduction state has been recently studied by Chang and Lou[16]. Specifically, we focus on a model colloidal HgTe quantum disk with radius R and height H in vacuum, shown schematically in the inset to Fig. 2(a). The single-particle energy levels and the corresponding wave functions as a function of strain applied along the disk height are computed in the eight-band $\vec{k} \cdot \vec{p}$ approach with the HgTe material parameters, described in detail in the Methods section and taken from Ref. 24.

The eight-band $\vec{k} \cdot \vec{p}$ bulk Hamiltonian is written in the basis of two conduction and six valence subband states. The eigenstates of the Hamiltonian are spinors with chirality up or down (see Methods section). Each spinor carries conduction band, heavy hole, light hole and spin split-off band components with a specific angular momenta for in-plane motion and parity for vertical motion. The chirality is a good quantum number and allows for the rigorous classification of quantum states as observed experimentally by Doty $et\ al$[21,22]. For example, we write the spinor with chirality "up" in the form

$$
|\Uparrow, L\rangle =
\begin{bmatrix}
\sum\limits_{n=1}^{N}\sum\limits_{l=0}^{M} A_{nl}^{(1)} |n, m+1, 2l+1\rangle |S\uparrow\rangle \\[4pt]
\sum\limits_{n=1}^{N}\sum\limits_{l=0}^{M} A_{nl}^{(2)} |n, m+2, 2l\rangle |S\downarrow\rangle \\[4pt]
\sum\limits_{n=1}^{N}\sum\limits_{l=0}^{M} A_{nl}^{(3)} |n, m, 2l+1\rangle \left|\tfrac{3}{2}, +\tfrac{3}{2}\right\rangle \\[4pt]
\sum\limits_{n=1}^{N}\sum\limits_{l=0}^{M} A_{nl}^{(4)} |n, m+1, 2l\rangle \left|\tfrac{3}{2}, +\tfrac{1}{2}\right\rangle \\[4pt]
\sum\limits_{n=1}^{N}\sum\limits_{l=0}^{M} A_{nl}^{(5)} |n, m+2, 2l+1\rangle \left|\tfrac{3}{2}, -\tfrac{1}{2}\right\rangle \\[4pt]
\sum\limits_{n=1}^{N}\sum\limits_{l=0}^{M} A_{nl}^{(6)} |n, m+3, 2l\rangle \left|\tfrac{3}{2}, -\tfrac{3}{2}\right\rangle \\[4pt]
\sum\limits_{n=1}^{N}\sum\limits_{l=0}^{M} A_{nl}^{(7)} |n, m+1, 2l\rangle \left|\tfrac{1}{2}, +\tfrac{1}{2}\right\rangle \\[4pt]
\sum\limits_{n=1}^{N}\sum\limits_{l=0}^{M} A_{nl}^{(8)} |n, m+2, 2l+1\rangle \left|\tfrac{1}{2}, -\tfrac{1}{2}\right\rangle
\end{bmatrix}, \qquad (1)
$$

where, $|n, m\rangle$ denote the in-plane basis functions with radial node number n and angular momentum m, $|2l+1\rangle$ ($|2l\rangle$) describe the even (odd) trigonometric functions in the z-direction, $|J, J_z\rangle$ are the sub-band microscopic (Bloch) functions, and $A_{nl}^{(i)}$ are expansion coefficients (see the Methods section). We see that the spinor contains all conduction band and valence band states and that the different sub-band components enter with different angular momentum and parity. This spinor is characterized by the total angular momentum quantum number $L = m + \tfrac{3}{2}$ which is a sum of the orbital angular momentum m and the z-projection of the Bloch angular momentum J. We have chosen to define the angular momenta of all spinor components relative to the number m of the heavy-hole component. In a similar way we define chirality "down" spinors. The eight-band $\vec{k} \cdot \vec{p}$ Hamiltonian is expanded in the basis of spinors and diagonalized to obtain coefficients A as explained in the Methods section. The wave functions vanish at the edge of the disk and any state localized

at the edge must be characterized by its effective radius R^* and decay into the disk. Obtaining such localized states in terms of our basis functions is a nontrivial numerical task.

First we search for an optimal height H of the HgTe quantum well close to the transition from the normal semiconductor to the topological insulator, i.e., from the normal to the inverted bandgap regime. Figure 2(a) shows the energies of the quantum well subbands in the vicinity of the critical thickness H_C, where the conduction band edge belonging to the lowest subband (denoted in blue) crosses the lowest-subband heavy-hole band edge (denoted in red). Thus, at sufficiently small well thicknesses H we deal with the normal semiconductor phase with the positive bandgap, while at larger well thicknesses the material exhibits a bulk-like, inverted bandstructure. The critical thickness for the infinite HgTe quantum well surrounded by vacuum is found at $H_C = 3.4$ nm. Here, the in-plane dispersion corresponds to a single Dirac cone as discussed and observed for HgTe/CdTe quantum well[13]. This Dirac cone is presented in Fig. 2(b).

We now turn to a quantum disk with a height of $H = 4$ nm which corresponds to a quantum well in the TI regime. We unfold our spinors in linear combinations of N Bessel functions and M sines for each subband, which results in the Hamiltonian matrix of order of $K = 8NM$ for each total angular momentum and chirality channel. In Fig. 3(a) we show the eigenenergies of the quantum disk obtained without strain by diagonalizing the Hamiltonian matrix with $N = 40$ and $M = 10$. The levels, denoted by red and blue bars for chirality "up" and "down", respectively, are plotted against the total angular momentum L. The states form degenerate Kramers pairs, one with chirality "up", and the other with chirality "down", characterized by opposite total angular momenta. We see the formation of two bands of edge states with quasi-linear dispersion, the band with chirality "up" decreasing in energy as the total angular momentum is increased, and the band with chirality "down" behaving oppositely. Further, at energies higher than the edge bands we find the "interior" (non-edge) electron states, resembling those found in the NS quantum dot. The "interior" heavy-hole states form a ladder of levels below the edge bands.

Fig. 3(b) illustrates the effect of strain included via the Bir-Pikus Hamiltoninan on the single-particle energies. The compression $\varepsilon = -0.02$ along the disk height shifts differently the electron and hole levels and tunes the HgTe bandgap, such that its increase is analogous to moving from right to left in Fig. 2(a). This results in a wider energy gap in the quantum dot spectrum and removal of the edge states.

We now discuss how the strain induced transition from a state with edge states in the energy gap to the insulating state without such states might be detected in transport. The two horizontal lines visible in Fig. 3(a) and (b) denote the conduction window $\Delta E_{SD} = eV_{SD}$, where V_{SD} is the source-drain voltage, defined by the Fermi levels of the left (L) and right (R)leads. The number M of edge states with the energy found within this window contributes to the tunneling of electrons from one lead to the other, and current $I = G_0 MTV_{SD}$ as discussed in the introduction. With our choice of the ΔE_{SD}, at zero strain we find six states, while at $\varepsilon = -0.02$ the conduction window is empty and the tunneling current cannot flow. In Fig. 3(c) we show the effect of the width of the source-drain voltage window on the number M of available conduction channels as a function of the strain. Different curves correspond to different source-drain voltages. We see that a small conduction window contains fewer edge states, exhibits a low critical strain and an abrupt transition from the "on" to "off" state. This is the quantitative illustration of the central result of our work presented in Fig. 1. As the conduction window increases, the "on" current increases due to the increased number of conduction channels, and the transition to the "off" regime is less abrupt, consists of steps, and exhibits a larger critical strain. We expect, therefore, that the sensitivity and signal-to-noise ratio can be significantly tuned simply by changing the source-drain voltage of the leads. The effect discussed here is to be contrasted with piezo-
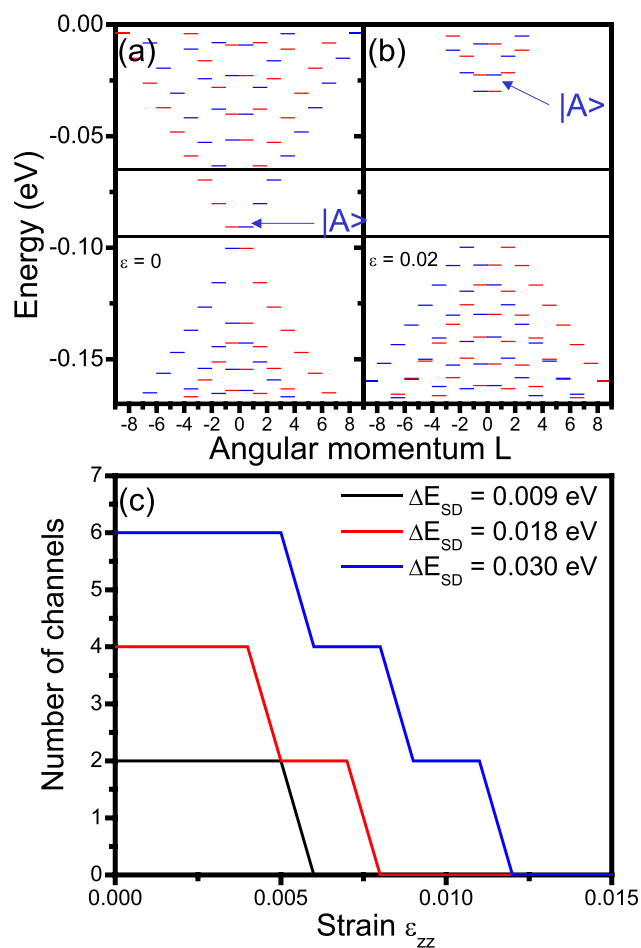

Figure 3 | Single-particle states of the quantum disk of height $H = 4$ nm and vertical strain $\varepsilon_{zz} = 0$ (a), and $\varepsilon_{zz} = -0.02$ (b). The black horizontal lines define the conduction window established by the Fermi levels of the leads of the electrical strain detector. Red (blue) bars correspond to chirality "up" ("down"). Panel (c) shows the current flowing through the sensor, measured in terms of the number of conduction channels, as a function of the strain. Different curves correspond to different widths of the conduction window.

electric sensors where induced charge is a linear function of applied pressure[5–7], but has analogies to single-electron charge detection using conductance steps in quantum point contacts[1,2] and pressure induced metal-insulator transitions in thin films[8]. The magnitude of strain of few percent is comparable to strains detected using piezoelectric semiconductor nanowires[6].

We conclude our proposal by demonstrating that not only the number, but also the nature of the conduction channels changes with the strain. In Fig. 4 we show the radial dependence of the probability densities of the state denoted in Fig. 3 as $|A\rangle$. The panels show, respectively, the electron (red) and heavy-hole (blue) component of this state. We see that as the strain is increased, the probability density of the electronic component evolves from one peaked at the edge to one peaked in the interior of the disk, while the hole component drops to zero. Thus, as expected, the states begin to resemble those of the NS quantum disk. As the probability density moves to the center, the tunneling from the leads onto the conduction channels decreases exponentially. Therefore, even though a state may be still within the conduction window, its contact to leads (tunneling matrix element), and therefore the tunneling current, decreases as a function of stress.

In conclusion, we present a microscopic theory of a HgTe quantum dot as a function of size and applied strain. We demonstrated the existence of edge states and their removal with applied

strain. We propose that this mechanism could be used to implement a nanoscale, all-electrical, low-energy strain sensing device, in which the presence of a strain beyond a threshold value could be detected electrically as a collapse of the tunneling current through the edge states of the HgTe quantum disk.

Methods

The essential physics of the TI edge states can only be captured if one accounts for the strong mixing of the electron and hole subbands[9–11,28–30]. Here we analyze the single-particle properties of a HgTe disk, both free-standing and embedded in a normal semiconductor material in the eight-band $\vec{k}\cdot\vec{p}$ approach. This allows to relate its electronic properties directly to its geometric and material properties. Building on our previous work with NS quantum wells[31] and dots[20–23], we consider a HgTe quantum disk, shown schematically in the inset to Fig. 2(a). Here we discuss a free-standing nanocrystal, i.e., one whose surface is modeled simply as an infinite potential barrier. However, similar results were obtained for a HgTe quantum disk embedded in the CdTe barrier material. We take the radius of $R = 55$ nm and vary the height H from 2 nm to about 10 nm. As already mentioned, in our calculations we employ the eight-band $\vec{k}\cdot\vec{p}$ approach. The Hamiltonian and relevant HgTe material parameters, described in detail in the following, are taken from Ref. 24. We note that a strictly two-dimensional model of the HgTe dot has been considered in Ref. 16. In that approach, the effects of the disk height and subband mixing were accounted for only through effective parameters of the electron and the heavy hole in a two-band approach, which made its results difficult to relate directly to realistic structure parameters.

The eight-band $\vec{k}\cdot\vec{p}$ bulk Hamiltonian is written in the basis of two conduction and six valence subbands. Denoting the spin of the quasiparticle with an arrow, $\sigma = \uparrow(\downarrow) = \pm 1/2$, the Bloch basis set is chosen in the following form:

$$\langle \vec{r}|S,+1/2\rangle = S\uparrow, \tag{2}$$

$$\langle \vec{r}|S,-1/2\rangle = S\downarrow, \tag{3}$$

$$\langle \vec{r}|3/2,+3/2\rangle = \left(1/\sqrt{2}\right)(X+iY)\uparrow, \tag{4}$$

$$\langle \vec{r}|3/2,+1/2\rangle = \left(1/\sqrt{6}\right)[(X+iY)\downarrow - 2Z\uparrow], \tag{5}$$

$$\langle \vec{r}|3/2,-1/2\rangle = -\left(1/\sqrt{6}\right)[(X-iY)\uparrow + 2Z\downarrow], \tag{6}$$

$$\langle \vec{r}|3/2,-3/2\rangle = -\left(1/\sqrt{2}\right)(X-iY)\downarrow, \tag{7}$$

$$\langle \vec{r}|1/2,+1/2\rangle = \left(1/\sqrt{3}\right)[(X+iY)\downarrow + Z\uparrow], \tag{8}$$

$$\langle \vec{r}|1/2,-1/2\rangle = \left(1/\sqrt{3}\right)[(X-iY)\uparrow - Z\downarrow]. \tag{9}$$

The total Bloch angular momentum for the electron subbands (the first two states) is equal to the spin and is 1/2. The total Bloch angular momentum for the hole states is 3/2 for the heavy and light hole subbands, and 1/2 for the spin-orbit split-off subbands, and its projections are indicated by the second quantum number in the ket.

The bulk Hamiltonian written in this basis takes the following form:

$$H = \begin{pmatrix} \hat{T} & 0 & -\frac{1}{\sqrt{2}}P\hat{k}_+ & \sqrt{\frac{2}{3}}P\hat{k}_z & \frac{1}{\sqrt{6}}P\hat{k}_- & 0 & -\frac{1}{\sqrt{3}}P\hat{k}_z & -\frac{1}{\sqrt{3}}P\hat{k}_- \\ 0 & \hat{T} & 0 & -\frac{1}{\sqrt{6}}P\hat{k}_- & \sqrt{\frac{2}{3}}P\hat{k}_z & \frac{1}{\sqrt{2}}P\hat{k}_+ & -\frac{1}{\sqrt{3}}P\hat{k}_- & \frac{1}{\sqrt{3}}P\hat{k}_z \\ -\frac{1}{\sqrt{2}}P\hat{k}_- & 0 & \hat{U}+\hat{V} & -\hat{S}_- & \hat{R} & 0 & \frac{1}{\sqrt{2}}\hat{S}_- & -\sqrt{2}\hat{R} \\ \sqrt{\frac{2}{3}}P\hat{k}_z & -\frac{1}{\sqrt{6}}P\hat{k}_- & -\hat{S}_+^\dagger & \hat{U}-\hat{V} & 0 & \hat{R} & \sqrt{2}\hat{V} & -\sqrt{\frac{3}{2}}\hat{S}_- \\ \frac{1}{\sqrt{6}}P\hat{k}_+ & \sqrt{\frac{2}{3}}P\hat{k}_z & \hat{R}^\dagger & 0 & \hat{U}-\hat{V} & \hat{S}_- & -\sqrt{\frac{3}{2}}\hat{S}_+ & -\sqrt{2}\hat{V} \\ 0 & \frac{1}{\sqrt{2}}P\hat{k}_+ & \hat{R}^\dagger & \hat{S}_+^\dagger & \hat{U}+\hat{V} & \sqrt{2}\hat{R}^\dagger & \frac{1}{\sqrt{2}}\hat{S}_+ \\ -\frac{1}{\sqrt{3}}P\hat{k}_z & -\frac{1}{\sqrt{3}}P\hat{k}_- & \frac{1}{\sqrt{2}}\hat{S}_-^\dagger & \sqrt{2}\hat{V} & -\sqrt{\frac{3}{2}}\hat{S}_+^\dagger & \sqrt{2}\hat{R} & \hat{U}-\Delta & 0 \\ -\frac{1}{\sqrt{3}}P\hat{k}_+ & \frac{1}{\sqrt{3}}P\hat{k}_z & -\sqrt{2}\hat{R}^\dagger & -\sqrt{\frac{3}{2}}\hat{S}_+^\dagger & -\sqrt{2}\hat{V} & \frac{1}{\sqrt{2}}\hat{S}_+^\dagger & 0 & \hat{U}-\Delta \end{pmatrix} \tag{10}$$

The operators appearing in the above matrix are defined as:

$$\hat{T} = E_c + \frac{\hbar^2}{2m_0}\left(\hat{k}_x^2 + \hat{k}_y^2 + \hat{k}_z^2\right), \tag{11}$$

$$\hat{U} = E_v - \frac{\hbar^2}{2m_0}\gamma_1\left(\hat{k}_x^2 + \hat{k}_y^2 + \hat{k}_z^2\right), \tag{12}$$

$$\hat{V} = -\frac{\hbar^2}{2m_0}\gamma_2\left(\hat{k}_x^2 + \hat{k}_y^2 - 2\hat{k}_z^2\right), \tag{13}$$

$$\hat{R} = \sqrt{3}\frac{\hbar^2}{2m_0}\left[\gamma_2\left(\hat{k}_x^2 - \hat{k}_y^2\right) - 2i\gamma_3\hat{k}_x\hat{k}_y\right], \tag{14}$$

$$\hat{S}_\pm = -2\sqrt{3}\frac{\hbar^2}{2m_0}\gamma_3\hat{k}_\pm\hat{k}_z, \tag{15}$$

and $\hat{k}_\pm = \hat{k}_x \pm i\hat{k}_y$. Further, m_0 is the mass of a free electron and $\hbar$ is the Dirac constant. In what follows we take the following HgTe material parameters[24]: $\gamma_1 = 4.1$, $\gamma_2 = 0.5$, $\gamma_3 = 1.3$, the spin-orbit splitting $\Delta = 1.08$ eV, and the bandgap $E_g = E_c - E_v = -0.303$ eV, appropriate for our negative-badgap material. The conduction-valence subband coupling parameter P can be deduced from the Kane energy $E_P = 2m_0P^2/\hbar^2 = 18.8$eV. Lastly, we adopt the axial-symmetric approximation in which $\bar{\gamma} = (\gamma_2 + \gamma_3)/2$ and the operator $\hat{R}$ can be written in a simpler form $\hat{R} = \sqrt{3}\frac{\hbar^2}{2m_0}\bar{\gamma}\hat{k}_-^2$. The Hamiltonian (10) is applied to the zero-dimensional quantum disk by the usual substitution $\hat{k}_x = -i\partial/\partial x$, and analogously for coordinates y and z, and $\hat{k}_\pm = -ie^{\pm i\varphi}\left(\frac{\partial}{\partial r} \pm i\frac{1}{r}\frac{\partial}{\partial\varphi}\right)$. The natural choice of basis for the single-particle states consists of eigenvectors of the single-band Hamiltonian,

$$\langle \vec{r}|nml\rangle = \frac{\sqrt{2}}{P}\frac{1}{\left|J_{m+1}(\alpha_m^n)\right|}J_m\left(\alpha_m^n\frac{r}{P}\right)$$
$$\times \frac{1}{\sqrt{2\pi}}e^{im\varphi} \times \sqrt{\frac{2}{W}}\sin\left(l\pi\frac{z}{W}\right), \tag{16}$$

where J_m is the Bessel function of m-th order, and α_m^n is the n-th zero of that function. The quantum numbers $n = 0, 1, …, m = 0, \pm 1, \pm 2, …,$ and $l = 1, 2, …$ are, respectively, the nodal number and angular momentum of the in-plane function and the vertical subband index. Note that even (odd) values of l correspond to odd (even) vertical wave functions, with the origin of the coordinate system placed in the center of the base of the disk. The functions by construction vanish on all the surfaces of the disk, and therefore working with this basis we do not have to enforce any additional boundary conditions.

The eigenvectors of the Hamiltonian (10) are sought in the form of eight-component spinors, each component being a linear combination of single-subband functions. However, the analysis of symmetries of the Hamiltonian allows to discern two classes ("chiralities"), whose existence is related to the Kramers degeneracy. Owing to the fact that the operator $\hat{k}_+\left(\hat{k}_-\right)$ increases (decreases) the envelope angular momentum by one unit, and the operator $\hat{k}_z$ flips the symmetry of the vertical subband, we write the spinor with chirality "up" in the form presented in Eq. 1 (Refs. 20–22). This spinor is characterized by the total angular momentum quantum number $L = m + \frac{3}{2}$ which is a sum of the orbital angular momentum m and the z-projection of the Bloch angular momentum. We have chosen to define the angular momenta of all spinor components relative to the number m of the heavy-hole component. The spinor with chirality "down" takes the form

$$|\Downarrow,L\rangle = \begin{bmatrix} \sum_{n=1}^{N}\sum_{l=0}^{M} B_{nl}^{(1)}|n,m-2,2l\rangle|S\uparrow\rangle \\ \sum_{n=1}^{N}\sum_{l=0}^{M} B_{nl}^{(2)}|n,m-1,2l+1\rangle|S\downarrow\rangle \\ \sum_{n=1}^{N}\sum_{l=0}^{M} B_{nl}^{(3)}|n,m-3,2l\rangle|\frac{3}{2},+\frac{3}{2}\rangle \\ \sum_{n=1}^{N}\sum_{l=0}^{M} B_{nl}^{(4)}|n,m-2,2l+1\rangle|\frac{3}{2},+\frac{1}{2}\rangle \\ \sum_{n=1}^{N}\sum_{l=0}^{M} B_{nl}^{(5)}|n,m-1,2l\rangle|\frac{3}{2},-\frac{1}{2}\rangle \\ \sum_{n=1}^{N}\sum_{l=0}^{M} B_{nl}^{(6)}|n,m,2l+1\rangle|\frac{3}{2},-\frac{3}{2}\rangle \\ \sum_{n=1}^{N}\sum_{l=0}^{M} B_{nl}^{(7)}|n,m-2,2l+1\rangle|\frac{1}{2},+\frac{1}{2}\rangle \\ \sum_{n=1}^{N}\sum_{l=0}^{M} B_{nl}^{(8)}|n,m-1,2l\rangle|\frac{1}{2},-\frac{1}{2}\rangle \end{bmatrix}, \tag{17}$$

where N and M define respectively the total number of radial and vertical harmonics used in the calculation, and the total angular momentum $L = m - \frac{3}{2}$. The problem is
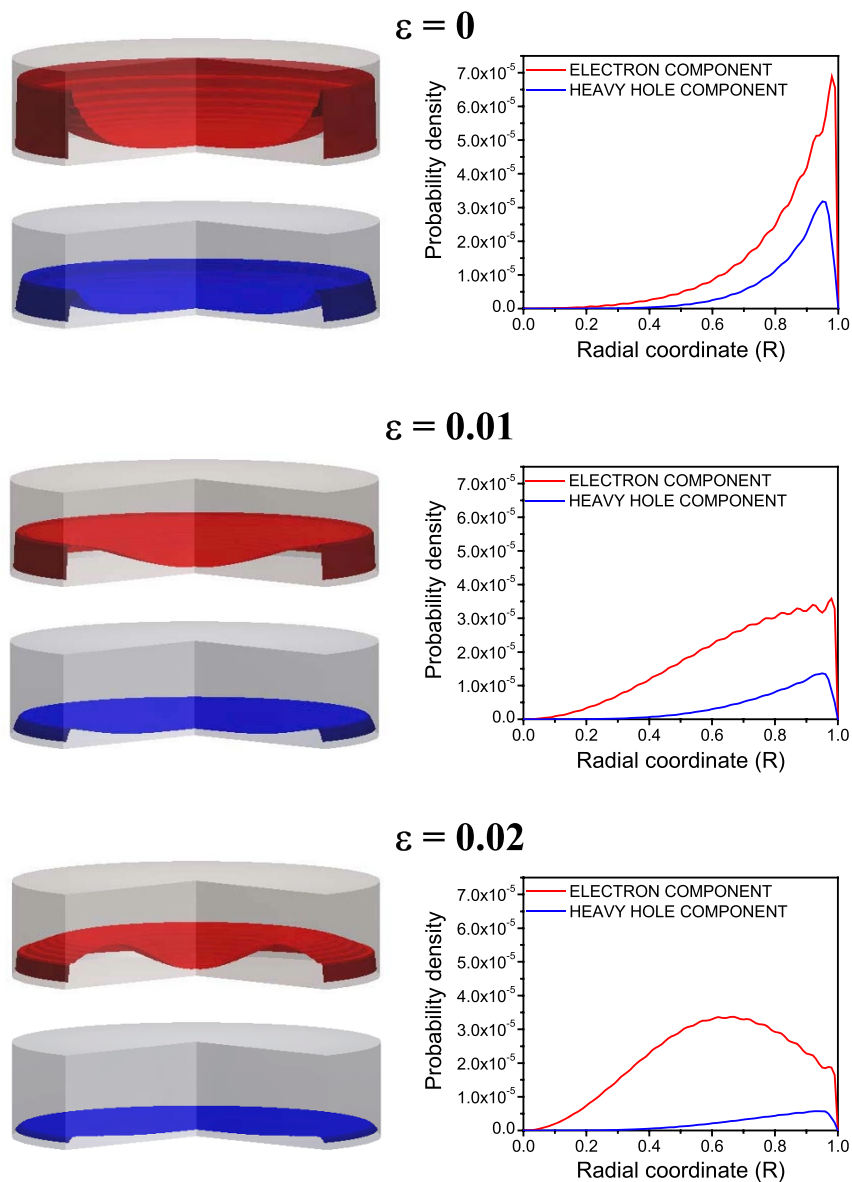
$$\varepsilon = 0$$

$$\varepsilon = 0.01$$

$$\varepsilon = 0.02$$

Figure 4 | Probability densities of the state $|A\rangle$ from Fig. 3 as a function of the radial coordinate for different applied strains. The electron and heavy hole wave function components are shown in red and blue, respectively, in the form of three-dimensional plots in the left-hand column. The radial plots along the x axis are shown on the right with the same colour code. Densities for the strain $\varepsilon = 0$, 0.01, and 0.02 are shown in the top, middle, and bottom panels, respectively.

thus reduced to finding the sets of coefficients $A_{nl}^{(i)}$ and $B_{nl}^{(i)}$ together with corresponding energy eigenvalues by diagonalizing numerically the Hamiltonian matrix set up in the above basis for each chirality, respectively.

Following Novik et al.[24] we account for the strain effects by means of the Bir-Pikus Hamiltonian which is added to the eight-band Hamiltonian, Eq. (10). In the above basis, this Hamiltonian takes the following form:

$$\hat{H}_{BP} = \begin{bmatrix} \hat{t} & 0 & 0 & 0 & 0 & 0 & 0 & 0 \\ 0 & \hat{t} & 0 & 0 & 0 & 0 & 0 & 0 \\ 0 & 0 & \hat{u}+\hat{v} & \hat{s} & \hat{r} & 0 & -\frac{1}{\sqrt{2}}\hat{s} & -\sqrt{2}\hat{r} \\ 0 & 0 & \hat{s}^+ & \hat{u}-\hat{v} & 0 & \hat{r} & \sqrt{2}\hat{v} & \sqrt{\frac{3}{2}}\hat{s} \\ 0 & 0 & \hat{r} & 0 & \hat{u}-\hat{v} & -\hat{s} & \sqrt{\frac{3}{2}}\hat{s}^+ & -\sqrt{2}\hat{v} \\ 0 & 0 & 0 & \hat{r}^+ & -\hat{s}^+ & \hat{u}+\hat{v} & \sqrt{2}\hat{r}^+ & -\frac{1}{\sqrt{2}}\hat{s}^+ \\ 0 & 0 & -\frac{1}{\sqrt{2}}\hat{s}^+ & \sqrt{2}\hat{v} & \sqrt{\frac{3}{2}}\hat{s} & \sqrt{2}\hat{r} & \hat{u} & 0 \\ 0 & 0 & -\sqrt{2}\hat{r}^+ & \sqrt{\frac{3}{2}}\hat{s}^+ & -\sqrt{2}\hat{v} & -\frac{1}{\sqrt{2}}\hat{s} & 0 & \hat{u} \end{bmatrix}, \quad (18)$$

with the following definitions of operators: $\hat{t} = a_c(\varepsilon_{xx} + \varepsilon_{yy} + \varepsilon_{zz})$,

$\hat{u} = a_v(\varepsilon_{xx} + \varepsilon_{yy} + \varepsilon_{zz})$, $\hat{v} = \frac{1}{2}b(\varepsilon_{xx} + \varepsilon_{yy} - 2\varepsilon_{zz})$, $\hat{s} = -d(\varepsilon_{xz} - i\varepsilon_{yz})$,

$\hat{r} = -\frac{\sqrt{3}}{2}b(\varepsilon_{xx} - \varepsilon_{yy}) + id\varepsilon_{xy}$. The strain defined by strain tensor matrix elements ε_{ij} is translated into energy via deformation potentials a_c, a_v, b, and d. In this work we utilize the values given by van de Walle[32]: $a_c = -4.60$ eV, $a_v = -0.13$ eV, and $b = -1.15$ eV. The value for the potential d is not needed as we do not consider any nondiagonal (shear) strain in the system.

In this work we consider a specific case of the disk being stressed in the vertical direction (along its thickness). We account for this case in the Bir-Pikus Hamiltonian, Eq. (18) by taking a nonzero strain tensor element $\varepsilon_{zz} = \Delta H/H$, describing the relative change of the dot height, and setting all other strain tensor matrix elements to zero. This approach neglects any buckling effects that might occur close to the edges of the disk. Under such simple strain, the only remaining nonzero elements of the Bir-Pikus Hamiltonian are $\hat{t}$, which renormalizes the conduction band edge, and $\hat{u}$ and $\hat{v}$, which influence the valence subbands. Specifically, if the disk is stressed compressively ($\varepsilon_{zz} < 0$), the conduction band edge is shifted towards higher energies, since the relevant deformation potential $a_c < 0$. The heavy-hole band edge undergoes the shift of $\hat{u} + \hat{v} = (a_v - b)\varepsilon_{xx}$. Both valence-band deformation potentials are negative, but the potential b is an order of magnitude larger than a_v. Under the negative strain, therefore, the heavy-hole subband edge is shifted towards lower energies. In total, the corrections to the conduction and heavy-hole band edges contribute a positive term

to the bandgap, i.e., tend to drive the system from the inverted regime towards the normally gapped regime. This property is the physical principle of operation of our strain sensor.

1. Elzerman, J. M. *et al.* Single-shot read-out of an individual electron spin in a quantum dot. *Nature* **430**, 431–435 (2004).
2. Granger, G. *et al.* Quantum interference and phonon-mediated back-action in lateral quantum-dot circuits. *Nature Phys.* **8**, 522–527 (2012).
3. Balasubramanian, G. *et al.* Nanoscale imaging magnetometry with diamond spins under ambient conditions. *Nature* **455**, 648–651 (2008).
4. Mamin, H. J. *et al.* Nanoscale Nuclear Magnetic Resonance with a Nitrogen-Vacancy Spin Sensor. *Science* **339**, 557–560 (2013).
5. Wang, X. *et al.* Piezoelectric Field Effect Transistor and Nanoforce Sensor Based on a Single ZnO Nanowire. *Nano Lett.* **6**, 2768–2772 (2006).
6. Wang, Z. L. Progress in Piezotronics and Piezo-Phototronics. *Adv. Materials* **24**, 4632 (2012).
7. Wu, W., Wen, X. & Wang, Z. L. Taxel-Addressable Matrix of Vertical-Nanowire Piezotronic Transistors for Active and Adaptive Tactile Imaging. *Science* **340**, 952–957 (2013).
8. Copel, M. *et al.* Giant Piezoresistive On/Off Ratios in Rare-Earth Chalcogenide Thin Films Enabling Nanomechanical Switching. *Nano Lett.* **13**, 4650 (2013).
9. Hasan, M. Z. & Kane, C. L. Colloquium: Topological insulators. *Rev. Mod. Phys.* **82**, 3045–3067 (2010).
10. Moore, J. E. The birth of topological insulators. *Nature* **464**, 194–198 (2010).
11. Qi, X.-L. & Zhang, S.-C. Topological insulators and superconductors. *Rev. Mod. Phys.* **83**, 1057–1110 (2011).
12. König, M. *et al.* Quantum Spin Hall Insulator State in HgTe Quantum Wells. *Science* **318**, 766–770 (2007).
13. Büttner, B. *et al.* Single valley Dirac fermions in zero-gap HgTe quantum wells. *Nature Phys.* **7**, 418–422 (2011).
14. Knez, I., Du, R. R. & Sullivan, G. Andreev Reflection of Helical Edge Modes in InAs/GaSb Quantum Spin Hall Insulator. *Phys. Rev. Lett.* **109**, 186603 (2012).
15. *Single Quantum dots: Fundamentals, Applications, and New Concepts*, edited by Michler, P. *Topics in Applied Physics* Vol. 90 (Springer-Verlag, Berlin, 2003).
16. Chang, K. & Lou, W.-K. Helical Quantum States in HgTe Quantum Dots with Inverted Band Structures. *Phys. Rev. Lett.* **106**, 206802 (2011).
17. Landauer, R. Electrical resistance of disordered one-dimensional lattices. *Phil. Mag.* **21**, 863 (1970); Büttiker, M. Four-terminal phase-coherent conductance. *Phys. Rev. Lett.* **57**, 1761 (1986).
18. Delgado, F. & Hawrylak, P. Theory of electronic transport through a triple quantum dot in the presence of magnetic field. *J. Phys.: Condens. Matter* **20**, 315207 (2008).
19. Shim, Y.-P., Delgado, F. & Hawrylak, P. Tunneling spectroscopy of spin-selective Aharonov-Bohm oscillations in a lateral triple quantum dot molecule. *Phys. Rev. B* **80**, 115305 (2009).
20. Rego, L. G. C., Hawrylak, P., Brum, J. A. & Wojs, A. Interacting valence holes in p-type SiGe quantum disks in a magnetic field. *Phys. Rev. B* **55**, 15694–15700 (1997).
21. Doty, M. F. *et al.* Antibonding Ground States in InAs Quantum-Dot Molecules. *Phys. Rev. Lett.* **102**, 047401 (2009).
22. Climente, J. I., Korkusinski, M., Goldoni, G. & Hawrylak, P. Theory of valence-band holes as Luttinger spinors in vertically coupled quantum dots. *Phys. Rev. B* **78**, 115323 (2008).
23. Korkusinski, M. & Hawrylak, P. Atomistic theory of emission from dark excitons in self-assembled quantum dots. *Phys. Rev. B* **87**, 115310 (2013).
24. Novik, E. G. *et al.* Band structure of semimagnetic $Hg_{1-y}Mn_yTe$ quantum wells. *Phys. Rev. B* **72**, 035321 (2005).
25. Lhuillier, E., Keuleyan, S. & Guyot-Sionnest, P. Optical properties of HgTe colloidal quantum dots. *Nanotechnology* **23**, 175705 (2012).
26. Keuleyan, S., Lhuillier, E. & Guyot-Sionnest, P. Synthesis of Colloidal HgTe Quantum Dots for Narrow Mid-IR Emission and Detection. *J. Am. Chem. Soc.* **133**, 16422–16424 (2011).
27. Zhang, X. W. & Xia, J. B. Electronic structure and electron g factors of HgTe quantum dots. *J. Phys. D* **39**, 1815 (2006).
28. Qi, X.-L., Hughes, T. L. & Zhang, S.-C. Topological field theory of time-reversal invariant insulators. *Phys. Rev. B* **78**, 195424 (2008).
29. König, M. *et al.* The Quantum Spin Hall Effect: Theory and Experiment. *J. Phys. Soc. Japan* **77**, 031007 (2008).
30. Zhou, B., Lu, H.-Z., Chu, R.-L., Shen, S.-Q. & Niu, Q. Finite Size Effects on Helical Edge States in a Quantum Spin-Hall System. *Phys. Rev. Lett.* **101**, 246807 (2008).
31. Rego, L. G. C., Brum, J. A. & Hawrylak, P. Multi-charged acceptor centers in p-doped $Si/Si_{1-x}Ge_x/Si$ quantum wells in the presence of a magnetic field. *Physica E* **2**, 785–788 (1998).
32. van de Walle, C. G. Band lineups and deformation potentials in the model-solid theory. *Phys. Rev. B* **39**, 1871–1883 (1989).

Author contributions

Additional information